AGU100 ADVANCING EARTH AND SPACE SCIENCE

JGR

Journal of Geophysical Research: Solid Earth

RESEARCH ARTICLE
10.1029/2018JB015504

Key Points:
- Theoretical equations for the displacement, velocity, and acceleration root-mean-square are derived, relying on the Brune omega-squared model
- Using these relations, source parameter inversion is performed in the time domain, producing stable and robust estimates
- Physics-based ground motion prediction equations are presented, exhibiting good agreement with previous empirical ones for all magnitudes

Correspondence to:
I. Lior,
itzhaklior22@gmail.com

Citation:
Lior, I., & Ziv, A. (2018). The relation between ground motion, earthquake source parameters, and attenuation: Implications for source parameter inversion and ground motion prediction equations. *Journal of Geophysical Research: Solid Earth*, *123*, 5886–5901. https://doi.org/10.1029/2018JB015504

Received 18 JAN 2018
Accepted 30 JUN 2018
Accepted article online 5 JUL 2018
Published online 25 JUL 2018

The Relation Between Ground Motion, Earthquake Source Parameters, and Attenuation: Implications for Source Parameter Inversion and Ground Motion Prediction Equations

Itzhak Lior[1] and Alon Ziv[1]

[1]Department of Geosciences, Tel Aviv University, Tel Aviv, Israel

Abstract Theoretical equations relating the root-mean-square (rms) of the far-field ground motions with earthquake source parameters and attenuation are derived for Brune's omega-squared model that is subject to attenuation. This set of model-based predictions paves the way for a completely new approach for earthquake source parameter inversion and forms the basis for new physics-based ground motion prediction equations (GMPEs). The equations for ground displacement, velocity, and acceleration constitute a set of three independent equations with three unknowns: the seismic moment, the stress drop, and the attenuation parameter. These are used for source parameter inversion that circumvents the time-to-frequency transformation. Initially, the two source parameters and the attenuation constant are solved simultaneously for each seismogram. Sometimes, however, this one-step inversion results in ambiguous solutions. Under such circumstances, the procedure proceeds to a two-step approach, in which a station-specific attenuation parameter is first determined by averaging the set of attenuation parameters obtained from seismograms whose one-step inversion yields well-constrained solutions. Subsequently, the two source parameters are solved using the averaged attenuation parameter. It is concluded that the new scheme is more stable than a frequency domain method, resulting in considerably less within-event source parameter variability. The above results together with rms-to-peak ground motion relations are combined to give first-order GMPEs for acceleration, velocity, and displacement. In contrast to empirically based GMPEs, the ones introduced here are extremely simple and readily implementable, even in low-seismicity regions, where the earthquake catalog lacks strong ground motion records.

1. Introduction

Resolving earthquake source parameters is key for addressing fundamental questions in earthquake science. The determination of earthquake source parameters is model based and is commonly done in the frequency domain using far-field records. The most widely adopted earthquake source model, describing the far-field body wave radiation, is that of Brune (Brune, 1970). According to Brune's model, the far-field ground motions read as

$$\frac{d^n}{dt^n}\Omega(f) = (2\pi f)^n \frac{\Omega_0}{1+\left(\frac{f}{f_0}\right)^2}, \tag{1}$$

where f is the frequency, f_0 is a corner frequency, and $n = 0$, 1, or 2 for displacement, velocity, or acceleration spectra, respectively. According to (1), the displacement spectra are constant and equal Ω_0 at frequencies well below the corner frequency and decay as f^{-2} above it (solid curves in top panels of Figure 1). The velocity spectra increase proportionally to f below the corner frequency and decrease as f^{-1} above it (solid curves in middle panels of Figure 1). Finally, the acceleration spectra rise as f^2 up to the corner frequency and are flat above it (solid curves in bottom panels of Figure 1). The spectral parameters Ω_0 and f_0 are related to the seismic moment, M_0, and the stress drop, $\Delta\tau$, as follows (Eshelby, 1957):

$$\Omega_0 = \frac{M_0 U_{\varphi\theta} F_s}{4\pi\rho C_S^3 R}, \tag{2a}$$

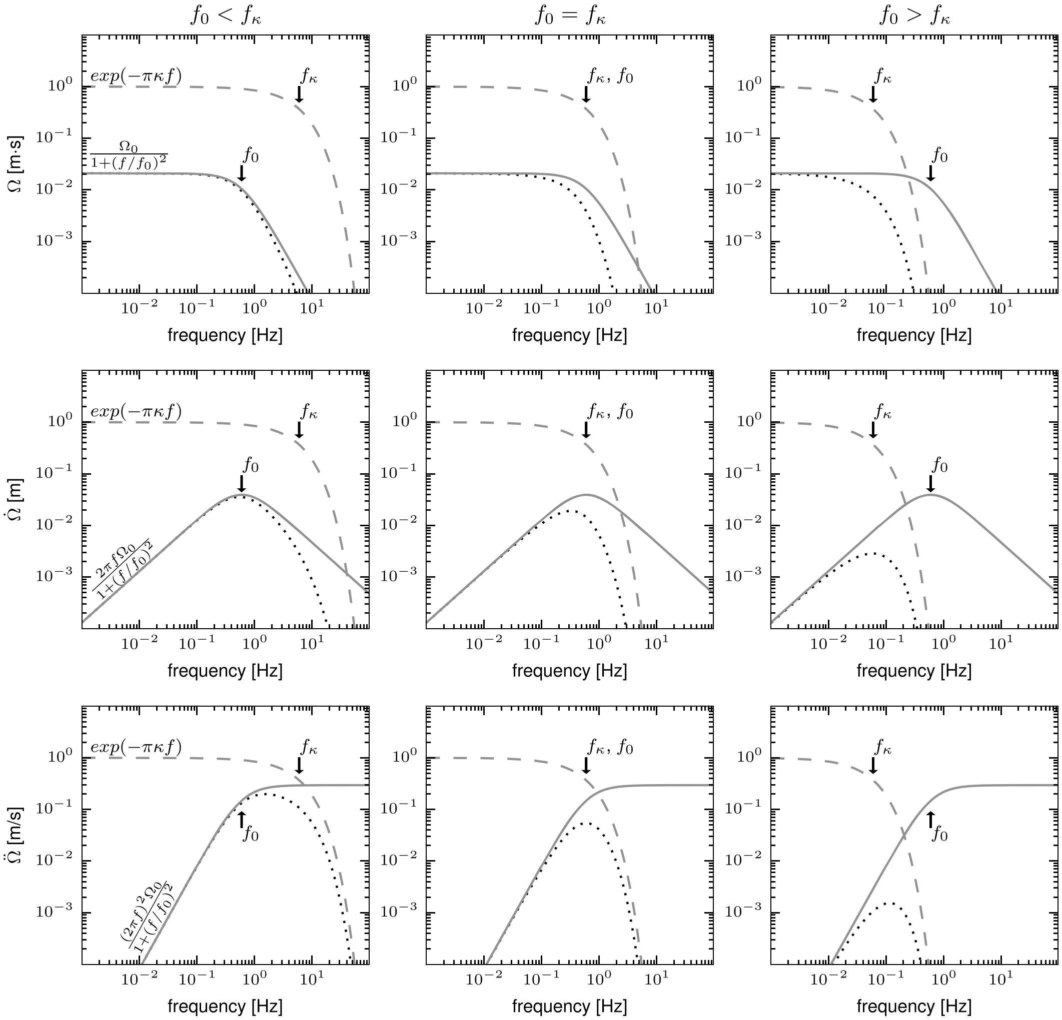

Figure 1. A set of diagrams illustrating the effect of near-site attenuation on the (top row) displacement, (middle row) velocity, and (bottom row) acceleration spectra of a synthetic earthquake (M_W = 5.5, $\Delta\tau$ = 10 MPa and R = 10 km). The source and the near-site attenuation models are indicated by solid and dashed lines, respectively, and their combined effect is indicated by dotted lines. Situations where $f_0 < f_\kappa$, $f_0 = f_\kappa$, and $f_0 > f_\kappa$ are shown in the left, middle, and right columns, respectively.

and:

$$f_0 = kC_S\left(\frac{16}{7}\frac{\Delta\tau}{M_0}\right)^{1/3}, \tag{2b}$$

where $U_{\varphi\theta}$ is the radiation pattern, F_s is the free-surface correction factor, C_S is the S wave velocity, R is the hypocentral distance, ρ is the density, and k is a constant (Brune, 1970; Madariaga, 1976; Sato & Hirasawa, 1973). Relation (2b) is valid for a circular crack embedded within an infinite homogeneous isotropic Poissonian medium. The effect of site and path attenuation can be modeled by multiplying the source spectra by an exponent function:

$$\frac{d^n}{dt^n}\Omega(f) = (2\pi f)^n \frac{\Omega_0}{1+\left(\frac{f}{f_0}\right)^2}\exp(-\pi\kappa f), \tag{3}$$

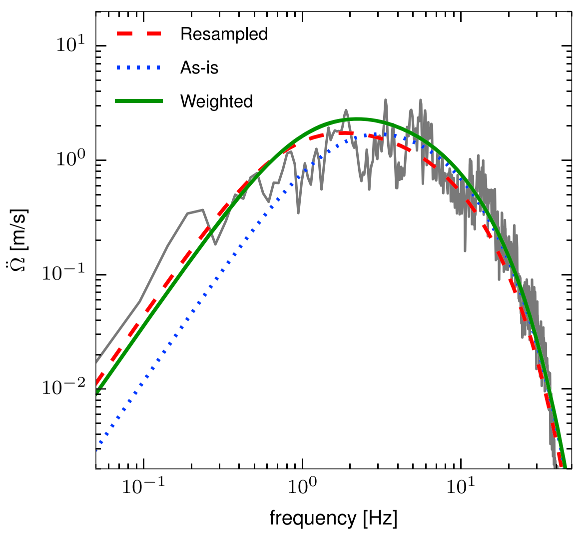

Figure 2. Comparison between different least-square fitting schemes. In all, the data (gray curve) are fitted to equation (3), with κ that is obtained from the acceleration spectra as in Anderson and Hough (1984). The dotted blue curve is the result of fitting the spectrum as is. The red dashed curve is the result of fitting the model to a spectrum that is resampled at constant log(f) units. The green solid curve is the result of fitting the spectrum using a weighted least squares fit, with weights that are inversely proportional to log(f).

where κ is an attenuation parameter that embodies both anelastic and near surface attenuations (Anderson & Hough, 1984). Positive κ results in a high-frequency decay of the spectra and effectively produces an additional corner frequency, f_κ (dashed curves in Figure 1; f_κ is referred to as f_{max} in Hanks, 1982):

$$f_\kappa = \frac{1}{\pi\kappa}. \tag{4}$$

In general, it is more difficult to resolve the spectral attributes when $f_0/f_\kappa > 1$ than $f_0/f_\kappa < 1$. To see why, it is useful to compare attenuated and nonattenuated earthquake spectra, with fixed Ω_0 and f_0 and varying f_0 to f_κ ratio (Figure 1). When f_0 is well below f_κ, the source spectra are only slightly attenuated (dotted curves in left-hand panels of Figure 1), and the source corner frequencies are well resolved. In contrast, when f_0 is larger than f_κ, the source spectra are more strongly distorted (right-hand panels of Figure 1), and consequently, the source corner frequencies can only be resolved if the attenuation parameters may be resolved as well. The f_0 to f_κ ratio is thus an important parameter affecting ground motion intensity and limiting the resolution of f_0. Hereafter this ratio is labeled as α_0:

$$\alpha_0 = f_0/f_\kappa = \pi\kappa f_0. \tag{5}$$

In this study, a new approach for seismic moment and stress drop inversion is introduced that circumvents the time-to-frequency data transformation. This is advantageous, since the modeling of ground motion spectra is nontrivial and introduces elements of subjectivity into the process. For example, some researchers resample the power spectrum coefficients at constant log of frequency units (e.g., Allmann & Shearer, 2009; Lior & Ziv, 2017; Ziv & Lior, 2016), some weight them proportionally to 1/ log (f) (e.g., Kaneko & Shearer, 2015; Trugman & Shearer, 2017), and some model them as is (e.g., Chen & Shearer, 2011; Prieto et al., 2004; Shearer et al., 2006). Because different schemes yield notably different results (Figure 2), seeking ways to bypass the biases inherited in the modeling of ground motion spectra is instructive.

Next, theoretical equations relating the root-mean-square (rms) of the far-field ground motions (displacement, velocity, and acceleration) to their spectral attributes are derived using the omega-squared model (Brune, 1970). These results, which constitute a set of three independent equations with three unknowns, are then used to invert for Ω_0, f_0, and κ. The trade-off between the effects of the source corner frequency and the attenuation parameter is quantified and addressed. The new inversion scheme is validated and assessed using an extensive data set of seismograms. It is shown that the new approach is more stable than a frequency domain inversion. Empirical relations between the peak ground motion and the rms of the ground motions are established. Finally, these empirical relations and the theoretical results for the ground motion rms are combined to give first-order ground motion prediction equations (GMPEs).

2. Far-Field Model

2.1. The Relation Between Ground Motion and Source Parameters

Lior and Ziv (2017) (hereafter referred to as LZ17) obtained expressions relating the rms of ground acceleration with the source parameters and κ (presented below for completeness). Their approach is now used to obtain equivalent expressions for the rms of the ground displacement and velocity. From Parseval's theorem, the ground motion rms can be calculated in both the time and the frequency domains:

$$y_{rms} = \sqrt{\frac{\int_{-\infty}^{\infty} |y(t)|^2 dt}{T}} = \sqrt{\frac{\int_{-\infty}^{\infty} |Y(f)|^2 df}{T}}, \tag{6}$$

where $y(t)$ is the ground motion time series, $Y(f)$ is the ground motion spectra, and T is the record interval. The displacement, velocity, and acceleration ground motion rms are obtained by substituting $Y(f)$ in (6) with equation (3):

$$\left(\frac{d^n}{dt^n}D\right)_{\mathrm{rms}} = \Omega_0\sqrt{\frac{2}{T}\int_0^\infty \frac{(2\pi f)^{2n}}{\left(1+\left(\frac{f}{f_0}\right)^2\right)^2}\exp(-2\pi\kappa f)df}. \tag{7}$$

The solutions of these integrals are

$$D_{\mathrm{rms}}^{\mathrm{exact}} = \Omega_0\sqrt{\frac{\alpha_0}{\pi^{3/2}\kappa T}}\sqrt{G_{1,3}^{3,1}\left(\left.\begin{matrix}\frac{1}{2}\\ 0,\frac{1}{2},\frac{3}{2}\end{matrix}\right|\alpha_0^2\right)}, \tag{8a}$$

$$V_{\mathrm{rms}}^{\mathrm{exact}} = 2\pi\Omega_0\left(\frac{\alpha_0}{(2T)^{1/3}\pi\kappa}\right)^{3/2}\sqrt{\begin{matrix}2Ci(2\alpha_0)[2\alpha_0\cos(2\alpha_0)+\sin(2\alpha_0)]+\\ [\pi-2Si(2\alpha_0)][\cos(2\alpha_0)-2\alpha_0\sin(2\alpha_0)]\end{matrix}}, \tag{8b}$$

$$A_{\mathrm{rms}}^{\mathrm{exact}} = (2\pi)^2\Omega_0\left(\frac{\alpha_0}{(2T)^{1/4}(\pi\kappa)^{5/4}}\right)^{2}\sqrt{\begin{matrix}2-2\alpha_0Ci(2\alpha_0)[2\alpha_0\cos(2\alpha_0)+3\sin(2\alpha_0)]+\\ [\pi\alpha_0-2\alpha_0Si(2\alpha_0)][2\alpha_0\sin(2\alpha_0)-3\cos(2\alpha_0)]\end{matrix}}, \tag{8c}$$

where D_{rms}, V_{rms}, and A_{rms} are the displacement, velocity, and acceleration rms, respectively, the superscript exact signifies exact solutions, G_{pq}^{mn} is the Meijer G-function, and Ci and Si are the cosine and the sine integral functions, respectively. As the rms of the ground motion may be calculated directly from the seismograms in the time domain, these three independent expressions can be used to invert for the spectral parameters Ω_0, f_0, and κ, without having to transform the data from the time to the frequency domain. Approximate expressions that match the exact solutions when $f_0 \ll f_\kappa$ and $f_0 \gg f_\kappa$ are as follows (the approach for approximating (8a)–(8c) is detailed in LZ17):

$$D_{\mathrm{rms}}^{\mathrm{approx}} = \Omega_0\sqrt{\frac{\pi}{2T}\frac{f_0}{1+0.5\pi^2\kappa f_0}}, \tag{9a}$$

$$V_{\mathrm{rms}}^{\mathrm{approx}} = 2\pi\Omega_0\sqrt{\frac{\pi}{2T}\left(\frac{f_0}{1+\pi^{4/3}\kappa f_0}\right)^3}, \tag{9b}$$

$$A_{\mathrm{rms}}^{\mathrm{approx}} = (2\pi)^2\Omega_0\frac{f_0^2}{\sqrt{\pi\kappa T}\left(1+1.5^{-1/4}\pi\kappa f_0\right)^2}, \tag{9c}$$

where the superscript approx signifies analytic approximations. Plots of exact and approximate solutions as a function of α_0 are shown in Figure 3 for D_{rms} and V_{rms} (see Figure 2 in LZ17 for A_{rms}). The discrepancies between the two solutions reach a few percent when $f_0{\sim}f_\kappa$. The approximate expressions in (9a)–(9c) may be expressed in terms of the physical source parameters M_0 and $\Delta\tau$, by substituting equations (2a) and (2b) into (9a)–(9c):

$$D_{\mathrm{rms}}^{\mathrm{approx}} = M_0^{5/6}\Delta\tau^{1/6}\frac{\beta_D}{\sqrt{T}R\left[1+0.5\pi^2\kappa kC_S\left(\frac{16\Delta\tau}{7M_0}\right)^{1/3}\right]^{1/2}}, \tag{10a}$$

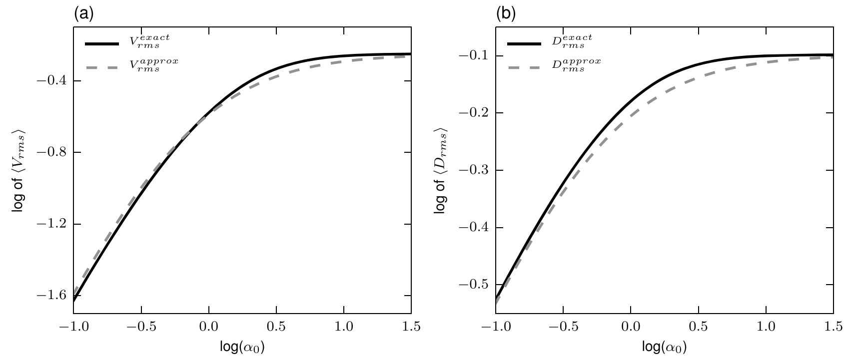

Figure 3. Comparison between the exact (equations (8a)–(8c), solid curves) and approximated solutions (equations (9a)–(9c), dashed curves). (a) The logarithm of the normalized displacement, $\langle D_{\rm rms}\rangle = D_{\rm rms}\sqrt{2\kappa T}/\Omega_0$, as a function of the logarithm of α_0. (b) The logarithm of the normalized velocity, $\langle V_{\rm rms}\rangle = V_{\rm rms}\sqrt{T}(\pi\kappa)^{1.5}/\left(\sqrt{2\pi}\pi\Omega_0\right)$, as a function of the logarithm of α_0.

$$V_{\rm rms}^{\rm approx} = \sqrt{M_0\Delta\tau}\frac{\beta_V}{\sqrt{T}R\left[1+\pi^{4/3}\kappa k C_S\left(\frac{16\Delta\tau}{7M_0}\right)^{1/3}\right]^{3/2}}, \tag{10b}$$

$$A_{\rm rms}^{\rm approx} = M_0^{1/3}\Delta\tau^{2/3}\frac{\beta_A}{\sqrt{\kappa T}R\left[1+1.5^{-1/4}\pi\kappa k C_S\left(\frac{16\Delta\tau}{7M_0}\right)^{1/3}\right]^{2}}, \tag{10c}$$

in which $\beta_D = U_{\varphi\theta}F_s(16/7)^{1/6}\sqrt{kC_S}/\left(\sqrt{2\pi}4\rho C_S^3\right)$, $\beta_V = 2\pi U_{\phi\theta}Fs\sqrt{16/7}(kC_S)^{3/2}/\left(\sqrt{2\pi}4\rho C_S^3\right)$, and $\beta_A = 4\pi U_{\phi\theta}$ $Fs(16/7)^{2/3}(kC_S)^2/\left(\sqrt{\pi}4\rho C_S^3\right)$. For large magnitudes, the second terms in the square brackets are much smaller than unity, and the above expressions simplify to

$$\lim_{\alpha_0\to 0} D_{\rm rms} = M_0^{5/6}\Delta\tau^{1/6}\frac{\beta_D}{\sqrt{T}R}, \tag{11a}$$

$$\lim_{\alpha_0\to 0} V_{\rm rms} = \sqrt{M_0\Delta\tau}\frac{\beta_V}{\sqrt{T}R}, \tag{11b}$$

$$\lim_{\alpha_0\to 0} A_{\rm rms} = M_0^{1/3}\Delta\tau^{2/3}\frac{\beta_A}{\sqrt{\kappa T}R}. \tag{11c}$$

In this regime, $D_{\rm rms}$ and $V_{\rm rms}$ (but not $A_{\rm rms}$) are insensitive to the attenuation. In contrast, for small magnitudes, the second terms in the square brackets are much larger than unity, and equations (10a)–(10c) simplify to

$$\lim_{\alpha_0\to\infty} D_{\rm rms} = M_0\frac{\beta_D}{\sqrt{T}R\left[0.5\pi^2\kappa k C_S(16/7)^{1/3}\right]^{1/2}}, \tag{12a}$$

$$\lim_{\alpha_0\to\infty} V_{\rm rms} = M_0\frac{\beta_V}{\sqrt{T}R\left[\pi^{4/3}\kappa k C_S(16/7)^{1/3}\right]^{3/2}}, \tag{12b}$$

$$\lim_{\alpha_0\to\infty} A_{\rm rms} = M_0\frac{\beta_A}{\sqrt{\kappa T}R\left[1.5^{-1/4}\pi\kappa k C_S(16/7)^{1/3}\right]^{2}}. \tag{12c}$$

In that case, the ground motion is insensitive to the stress drop. In a later section, the conditions described by equations (11a)–(11c) and (12a)–(12c) are referred to as the $\Delta\tau$-dependent and $\Delta\tau$-independent regimes, respectively.

2.2. Low-Frequency D_{rms} Correction

The finiteness of the data interval, the frequency above which the seismograms are high-passed, and the sensor's dynamic range set a lower limit on the signals' frequency content. In this study, the values of this cutoff frequency, denoted as f_l, are set to be equal to the largest of the following: the reciprocal of the data interval and the frequency above which the seismograms are high-passed. Among the three ground-motion rms in (9a)–(9c) and (10a)–(10c), D_{rms} is the one that is most affected by f_l. Thus, observed D_{rms} should be corrected for the missing low-frequency content:

$$D_{rms}^{obs+} = \sqrt{\left(D_{rms}^{obs}\right)^2 + \left(D_{rms}^{corr}\right)^2}, \tag{13}$$

with D_{rms}^{obs} and D_{rms}^{corr} being the observed rms and the correction term, respectively. Because under normal circumstances $f_l \ll f_\kappa$, attenuation does not affect frequencies below f_l, and the displacement correction term is obtained via solution of (1) and (6) as

$$D_{rms}^{corr} = \Omega_0 \sqrt{\frac{2}{T}\int_0^{f_l} \frac{1}{\left(1+\left(\frac{f}{f_0}\right)^2\right)^2} df} = \Omega_0 \sqrt{\frac{f_0}{T}\left[\frac{f_0 f_l}{f_0{}^2 + f_l{}^2} + \tan^{-1}\left(\frac{f_l}{f_0}\right)\right]}. \tag{14}$$

Finally, for $f_l \ll f_0$, the above expression may be approximated as

$$D_{rms}^{corr} = \Omega_0 \sqrt{\frac{f_l}{T}}. \tag{15}$$

3. Validation of Model Predictions

Model predictions are validated using a composite data set of 6,320 seismograms compiled by LZ17. Data selection criteria and processing steps are as in LZ17, except that here the high-pass filter is set to 0.06 instead of 0.02 Hz. Hypocentral distances and magnitudes are limited to 60 km and 3 to 7.6, respectively. As in LZ17, the data interval used in this study is set as: $T = 1/f_0 + R/C_S$. The first term is a liberal estimate of the rupture duration (Hanks & McGuire, 1981), with f_0 obtained from equation (2b) using the catalog magnitude and a stress drop of 1 MPa (this is merely used for setting the data interval, whereas the actual source corner frequency is later on calculated differently). The second term accounts for the spreading of the wave packet with distance from the earthquake source (Boore & Thompson, 2014). Here and in a later part of this study, results obtained using the new approach are compared to those calculated from the ground motion spectra. The frequency domain source parameter inversion is carried out in two steps. First, κ is obtained by fitting the high-frequency acceleration spectra to

$$\ln\left(\ddot{\Omega}(f)\right) = a - \pi\kappa f \quad ; \quad 10 \text{ Hz} < f < 25 \text{ Hz}, \tag{16}$$

with $\ddot{\Omega}(f)$ being the acceleration amplitudes and a and κ being the fitting coefficients (Anderson & Hough, 1984). Subsequently, Ω_0 and f_0 are obtained by fitting the logarithm of the acceleration spectra, resampled in equal log-of-frequency bins, with equation (3) using κ obtained in the first step.

The validation of the model prediction consists of comparing the observed ground motion rms, computed directly from the seismograms in the time domain, with equations (9a)–(9c) using Ω_0, f_0, and κ obtained

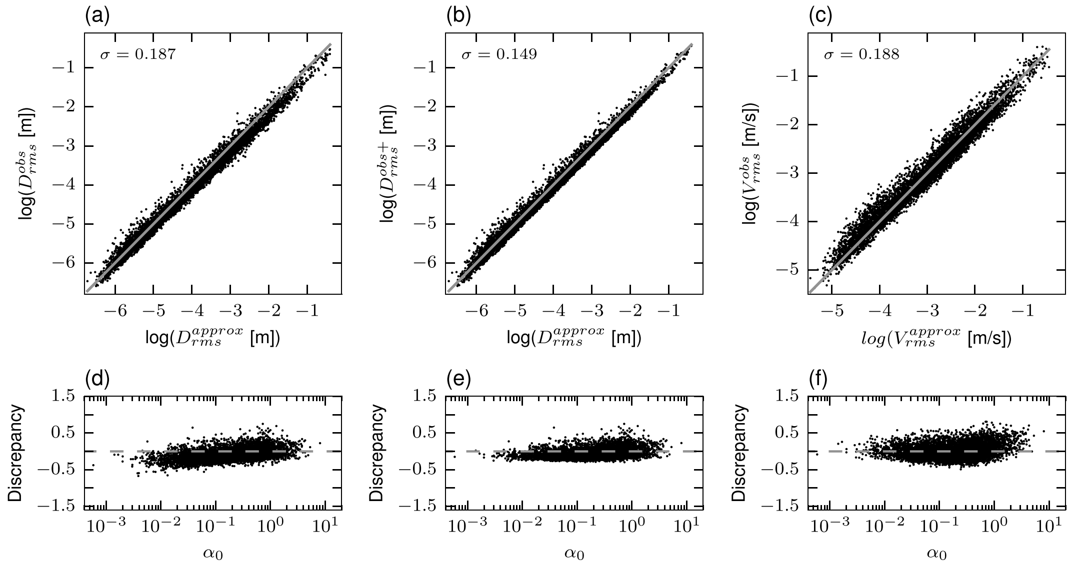

Figure 4. Observed versus predicted displacement and velocity rms. (a) The logarithms of $D_{\mathrm{rms}}^{\mathrm{obs}}$ as a function of the logarithm of $D_{\mathrm{rms}}^{\mathrm{approx}}$. (b) The logarithms of $D_{\mathrm{rms}}^{\mathrm{obs+}}$ as a function of the logarithm of $D_{\mathrm{rms}}^{\mathrm{approx}}$. (c) The logarithm of $V_{\mathrm{rms}}^{\mathrm{obs}}$ as a function of the logarithm of $V_{\mathrm{rms}}^{\mathrm{approx}}$. (d) $\log\left(D_{\mathrm{rms}}^{\mathrm{obs}}\right) - \log\left(D_{\mathrm{rms}}^{\mathrm{approx}}\right)$ as a function of α_0 (e) $\log\left(D_{\mathrm{rms}}^{\mathrm{obs+}}\right) - \log\left(D_{\mathrm{rms}}^{\mathrm{approx}}\right)$ as a function of α_0. (f) $\log\left(V_{\mathrm{rms}}^{\mathrm{obs}}\right) - \log\left(V_{\mathrm{rms}}^{\mathrm{approx}}\right)$ as a function of α_0.

from the frequency domain source parameter inversion. The results of this comparison for A_{rms} are shown and discussed in LZ17, and the results for the velocity and the corrected and uncorrected displacements are presented in Figure 4 (top panels). Also shown in Figure 4 (bottom panels) are the discrepancies between observed and modeled rms as a function of the ratio between the source corner frequency and the attenuation corner frequency, α_0. Inspection of Figure 4 reveals good agreement between modeled and observed ground motion rms. While the discrepancy of the uncorrected displacement rms increases with decreasing α_0 (bottom-left panel), that of the corrected displacement rms does not (bottom-middle panel). It is thus concluded that the displacement correction term is imperative, especially for low α_0 seismograms, which are generally rich in low frequencies.

4. Source Parameter Inversion Circumventing the Time-to-Frequency Data Transformation

4.1. General

The results detailed in the previous section pave the way for a source parameter inversion method that circumvents the time-to-frequency data transformation. Specifically, equations (8a)–(8c) constitute a set of three independent equations with three unknowns, in which the data vector is ($D_{\mathrm{rms}}^{\mathrm{obs+}}$, $V_{\mathrm{rms}}^{\mathrm{obs}}$, $A_{\mathrm{rms}}^{\mathrm{obs}}$), obtained in the time domain, and the model vector is (Ω_0, f_0, κ). The objective function, *OF*, used in this study is a measure of the discrepancy between the observed and the predicted ground motion rms:

$$OF = \max\left(\frac{\left|D_{\mathrm{rms}}^{\mathrm{obs+}} - D_{\mathrm{rms}}^{\mathrm{exact}}\right|}{D_{\mathrm{rms}}^{\mathrm{obs+}}}, \frac{\left|V_{\mathrm{rms}}^{\mathrm{obs}} - V_{\mathrm{rms}}^{\mathrm{exact}}\right|}{V_{\mathrm{rms}}^{\mathrm{obs}}}, \frac{\left|A_{\mathrm{rms}}^{\mathrm{obs}} - A_{\mathrm{rms}}^{\mathrm{exact}}\right|}{A_{\mathrm{rms}}^{\mathrm{obs}}}\right). \tag{17}$$

The three model parameters are solved simultaneously for each seismogram. Sometimes, however, this one-step inversion results in ambiguous solutions for f_0 and κ. Under such circumstances, the procedure proceeds to a two-step approach, in which a station-specific κ is first determined by averaging the set of κs obtained from seismograms whose one-step inversion yields well-constrained solutions, and then Ω_0 and f_0 are solved

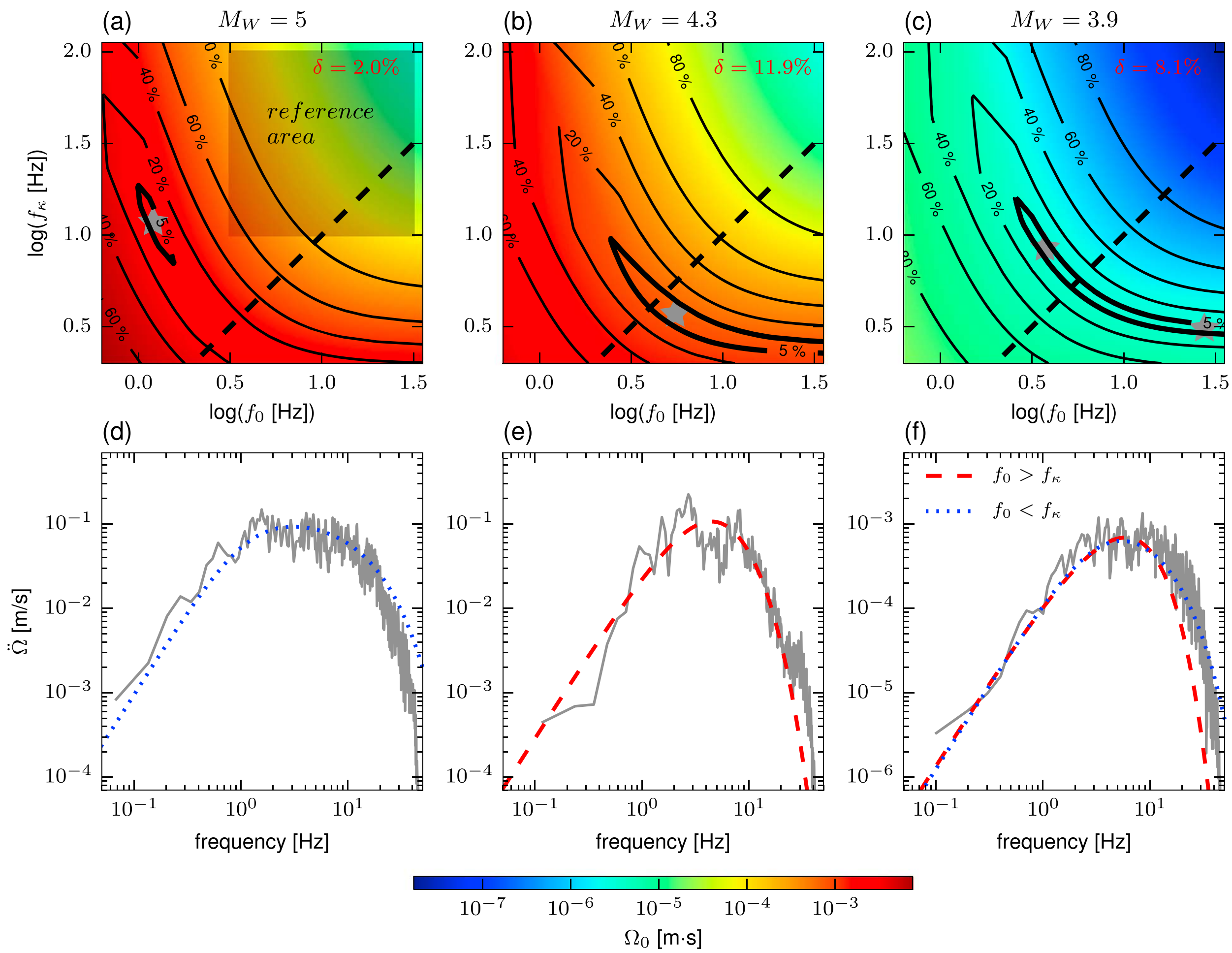

Figure 5. Plots of objective function and acceleration spectra corresponding to three example seismograms. (a–c) Contour diagrams of *OF* in log(f_0)-log(f_κ) space. The color code indicates optimal Ω_0, and the gray stars indicate *OF* minima. The uncertainty δ-parameter, reported at the top-right corner of each panel, is the area enclosed within the *OF* = 5% contour (thick contour), normalized by the gray shaded area shown in panel (a). The dashed lines indicate $f_0 = f_\kappa$. (d–f) The corresponding acceleration spectra are plotted in gray, along with the single-step solution (or solutions). The dashed red and dotted blue curves correspond to solutions for which $f_0 > f_\kappa$ and $f_0 < f_\kappa$, respectively.

using the averaged κ. The decision whether to proceed from a one-step to a two-step inversion is based on the quality of the one-step solution (further explained in the next section).

4.2. Single-Step Inversion

For each seismogram, a 3-D grid-search algorithm is employed that finds Ω_0, f_0, and κ corresponding to the smallest *OF* (equation (17)). To assess the robustness of this approach, it is useful to examine contour diagrams of the *OF* in log(f_0)-log(f_κ) space (Figure 5). In many cases, this approach yields one unique solution, which may be either well constrained (Figure 5a) or poorly constrained (Figure 5b). In some cases, however, the solutions are ambiguous with *OF* minima on either side of the $f_0 = f_\kappa$ line (Figure 5c). In these situations, because the two solutions share similar Ω_0, their spectra are nearly identical up to the lowest corner frequency (i.e., min(f_0, f_κ)), at which they both peak, but differ in the rate of decay beyond that frequency (panel f of Figure 5). Thus, in addition to minimizing *OF*, it is also vital to quantify the degree of uncertainty in the f_0-f_κ space.

Poorly constrained solutions are identified using an uncertainty measure, δ, that is proportional to the normalized area enclosed within the *OF* = 5% contour in Figure 5 (top diagrams). The distribution of δ is

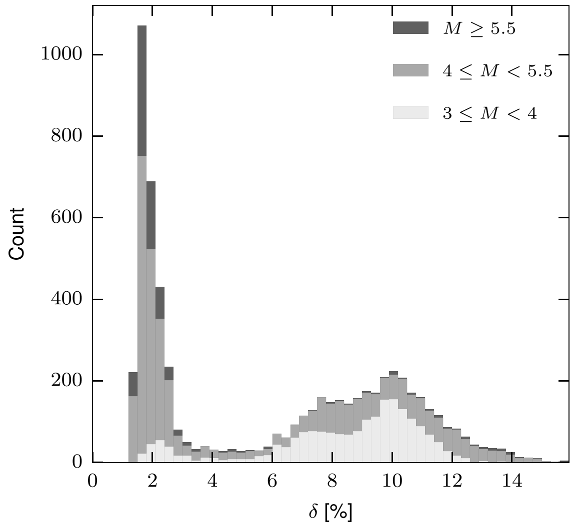

Figure 6. The distribution of seismogram-specific δ values according to magnitude bins.

bimodal, with the largest magnitudes residing mostly within the narrow peak around $\delta \approx 2\%$ and the smallest magnitude earthquakes residing mostly within the wider peak for which $\delta > 6\%$ (Figure 6). Yet there are quite a few exceptions, and each record should be examined individually regardless of its magnitude. Based on visual inspection of a large number of *OF* maps, such as those shown in Figure 5, it is concluded that single-step solutions are well constrained and unique if $\delta < 6\%$. It is interesting to compare Ω_0 and f_0 obtained using the new single-step approach with those obtained using the frequency domain approach (Figure 7). The new single-step inversion and the frequency domain inversion yield similar Ω_0 estimates for any δ and similar f_0 estimates when $\delta < 6\%$. In cases where $\delta > 6\%$, further analysis is needed, and the inversion proceeds to a two-step approach.

4.3. Two-Step Inversion

A two-step inversion is invoked when the one-step approach returns poorly constrained solutions. The method rests on the premise that at short hypocentral distances, such as those considered in this study, the effect of anelastic path-dependent attenuation is negligible (e.g., Lior et al., 2015; Lior & Ziv, 2017; Wu et al., 2005; Wu & Zhao, 2006), and the observed attenuation is entirely due to near-site effects. Hereafter, in order to emphasize the confinement to near-field attenuation, κ is replaced by κ_0 (e.g., Ktenidou et al., 2014). Thus, site-specific κ_0 parameters are determined by averaging well-constrained κ_0 values, that is, those corresponding to $\delta < 6\%$. In the second step, a grid-search over the Ω_0-f_0 space is performed for all available records (regardless of their δ), with the values of κ_0 held fixed at the site-specific values. Thus, in addition to circumventing the time domain to frequency domain data transformation, the two-step inversion also addresses the ambiguity in the f_0-f_κ space.

A necessary condition for the well posedness of any inverse problem is that its solution be stable. In the context of source parameter inversion, the solution stability may be assessed by means of within-event variability analysis. Specifically, the inversion is stable if the source parameter estimates of different seismic records corresponding to the same earthquake yield similar solutions. A comparison between the within-event variability of the two-step inversion described above (top panels in Figure 8) and that of the frequency domain inversion (bottom panels in Figure 8) indicates an overall smaller within-event variability for the first. The reduction in the within-event variability is more pronounced for f_0 than for M_0 and is also more pronounced

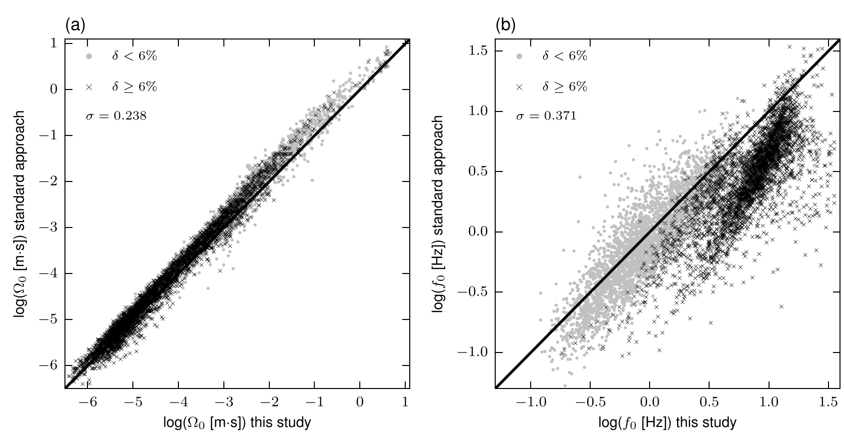

Figure 7. Comparison between the result of the frequency domain and the single-step schemes. (a) Ω_0 and (b) f_0 estimates. The gray circles and black "x" symbols correspond to seismograms with δ smaller than or greater than 6%, respectively.

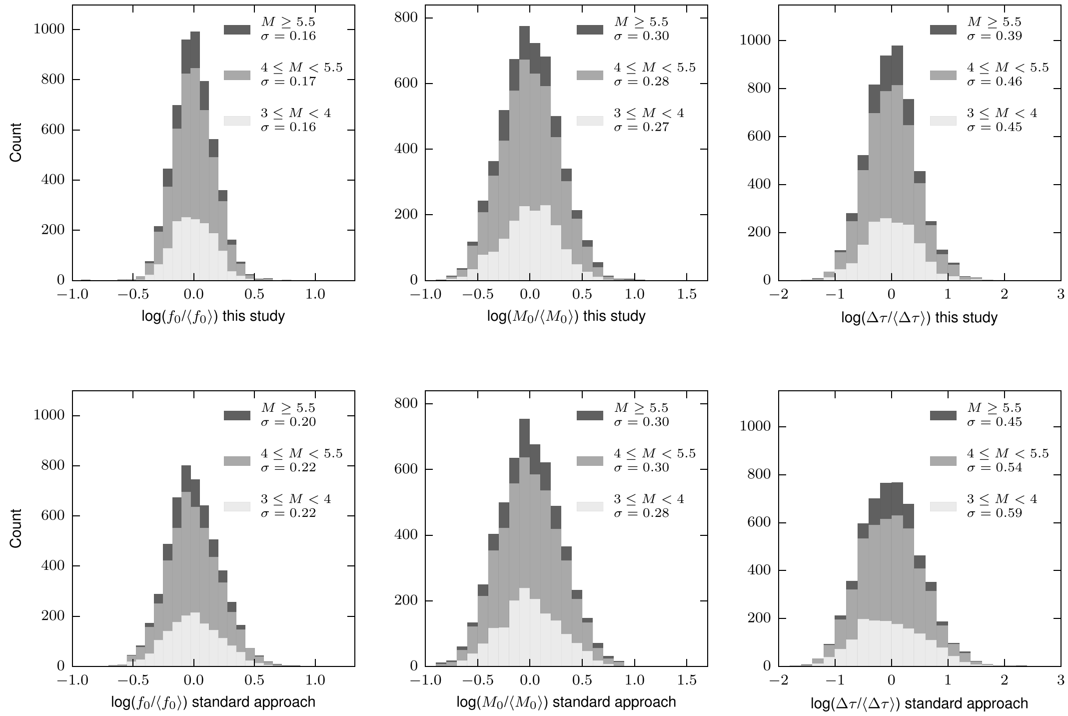

Figure 8. Comparison between within-event variability of f_0, M_0, and $\Delta\tau$ for the (top panels) two-step algorithm and the (bottom panels) frequency domain scheme. The distributions of within-event variabilities are shown according to three different magnitude bins for 444 earthquakes recorded by 4 or more stations. (left panels) The distribution of the logarithm of the corner frequency normalized by event-averaged corner frequency. (middle panels) The distribution of the logarithm of the seismic moment normalized by event-averaged seismic moment. (right panels) The distribution of the logarithm of the stress drop normalized by event-averaged stress drop. Standard deviations are reported on each panel.

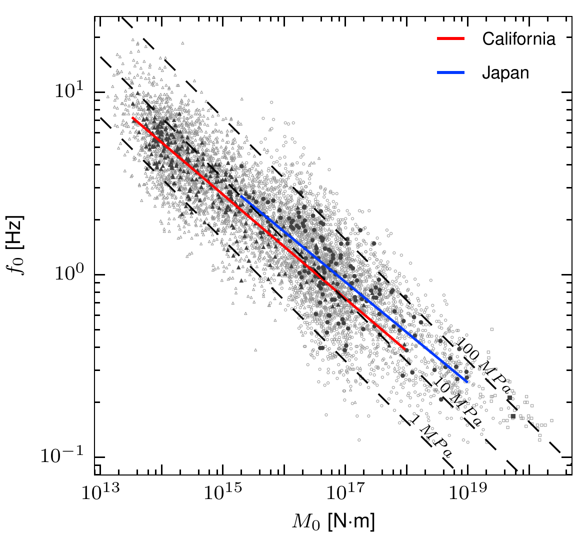

Figure 9. Log-log diagram of f_0 as a function of M_0. The gray and black dots correspond to seismogram-specific and event-average results, respectively. Least squares fits to the data for California and Japan are shown by red and blue curves, respectively.

for the smallest magnitudes than for the largest ones. The stress drops, being proportional to the product of M_0 and f_0^3 (equation (2b)), exhibit the largest within-event variability and the greatest improvement when switching from the frequency domain to the new two-step inversion. It is concluded that the new approach is more stable than a frequency domain inversion, and its within-event variability is well within the limits of the expected variability resulting from takeoff angle (Kaneko & Shearer, 2015; Madariaga, 1976; Sato & Hirasawa, 1973), radiation pattern (Dong & Papageorgiou, 2002; Kaneko & Shearer, 2015), irregular source geometry (Dong & Papageorgiou, 2002; Kaneko & Shearer, 2015), and propagation effects (Kaneko & Shearer, 2015; Ross & Ben-Zion, 2016).

A plot of the corner frequency as a function of the seismic moment is shown in Figure 9, along with lines of best fit for California and Japan (solid lines) that indicate a slight increase of stress drop with magnitude in both regions (using $k = 0.37$, as in Brune, 1970). The following stress drops versus seismic moment relations are inferred for California:

$$\log(\Delta\tau) = 4.57 + 0.14\log(M_0)(\pm 0.32), \tag{18a}$$

and Japan

$$\log(\Delta\tau) = 4.37 + 0.17\log(M_0)(\pm 0.45), \tag{18b}$$

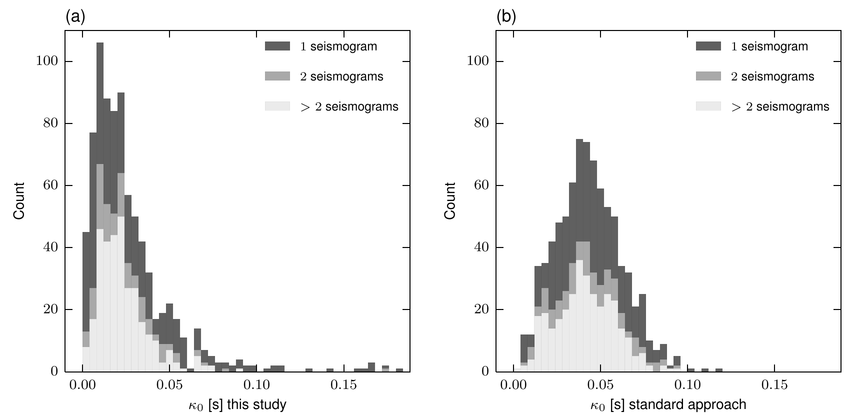

Figure 10. The distributions of station specific κ_0 for (a) the two-step inversion and (b) the frequency domain approach. Seismograms with $\delta > 6\%$ are excluded from these diagrams. The dark, medium and light gray correspond to stations whose κ values were averaged using 1, 2, or more than 2 seismograms, respectively.

with standard deviations reported in the parentheses. This trend is at odd with previous claims for self-similarity (e.g., Baltay et al., 2011; Ide et al., 2003; Ide & Beroza, 2001; Oth et al., 2010; Shearer et al., 2006) but is in line with recent studies from California and Japan (e.g., Drouet et al., 2011; Izutani & Kanamori, 2001; Mayeda et al., 2007; Takahashi et al., 2005; Trugman & Shearer, 2017). Furthermore, the stress drops are on average 85% larger in Japan than in California. As the data set from Japan is restricted to intraplate earthquakes, this result may be attributed to the generally higher stress drops observed in intraplate than in interplate earthquakes (e.g., Kanamori & Anderson, 1975; Leyton et al., 2009; Scholz et al., 1986). Given the strong dependency of the ground acceleration on the stress drop (equations (10a)–(10c)), these results are of importance for hazard assessment, as well as for understanding earthquake source physics in general.

The distribution of station-specific κ_0 arising from the new approach differs markedly from the one obtained using the frequency domain approach (Figure 10). While the first is of lognormal distribution with a median κ_0 around 0.028 s (mean log(κ_0)= -1.72 and σ= 0.39), the latter is close to a normal distribution with a larger median value of 0.043 s (mean κ_0= 0.043 s and σ= 0.019 s). Thus, the results of this study imply weaker near-site attenuation than previously estimated (Lior & Ziv, 2017; Oth et al., 2011; Van Houtte et al., 2011). The disparity between the two κ_0 distributions in Figure 10 is attributed mainly to differences in the bandwidths used by the two methods (e.g., Edwards et al., 2015; Mayor et al., 2018); while in Anderson and Hough (1984) κ is inferred from the acceleration spectra in a limited high-frequency band, here it is inferred from the full bandwidth of the three ground motion measures, that is, D_{rms}, V_{rms}, and A_{rms}.

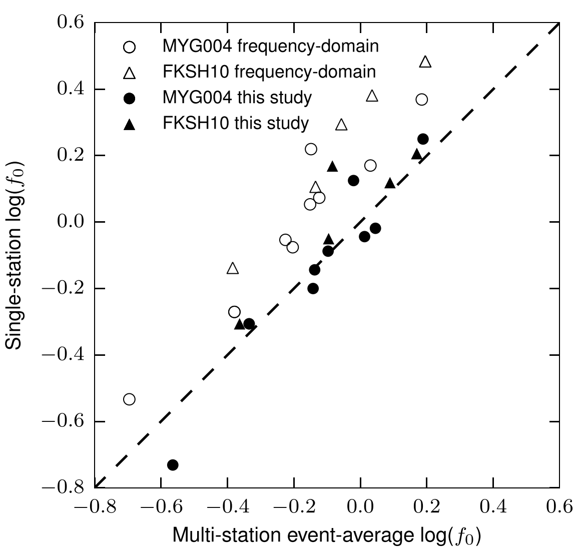

Figure 11. Comparison between single-station log(f_0) estimates at stations MYG004 (circles) and FKSH10 (triangles), where strong frequency-dependent site amplification has been reported (Nakano et al., 2015), and multiple-station event-average log(f_0). The empty and solid symbols indicate results of the frequency domain approach and the new two-step inversion, respectively.

The effect of frequency-dependent site amplification is not accounted for in equation (3), and consequently is neither explicitly addressed by the source parameter inversion introduced here, nor by the standard frequency domain approach. The performance of the inversion in the presence of such amplification is examined at two stations, MYG004 of K-net and FKSH10 of KiK-net, where strong high-frequency amplification has been reported (Nakano et al., 2015). A comparison between single-station log(f_0) estimates at these stations and multiple-station event-average log(f_0) is presented in Figure 11 for 14 earthquakes recorded at 11 and more stations. Good agreement between single- and multiple-station estimates is observed for the two-step approach. In contrast,

10.1029/2018JB015504

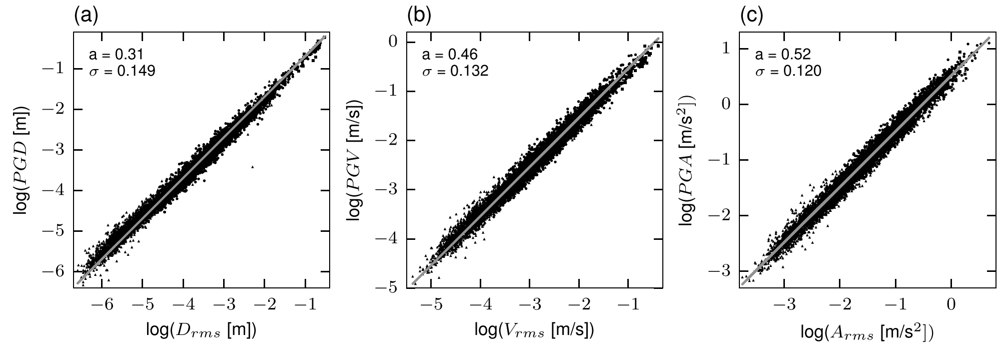

Figure 12. Peak versus rms ground motions. (a) log(PGD) as a function of log(D_{rms}). (b) log(PGV) as a function of log(V_{rms}). (c) log(PGA) as a function of log(A_{rms}). For consistency with common practices in earthquake engineering, the peak ground motions are the geometric mean of the peak motion of the two horizontal components. The gray line indicates a linear regression to: log(PG) = a + log (rms). The fitting coefficient, *a*, and the standard deviation are reported at the top left corner of each panel.

single-station f_0 estimates resulting from the frequency domain inversions are clearly biased toward higher frequencies. In addition to underlining the importance of using as many stations as possible, this result again indicates higher stability for the two-step time domain inversion than for the frequency domain inversion. It is further concluded that the ability of the two-step inversion to resolve the f_κ-f_0 ambiguity is not limited to favorable site conditions.

5. New Ground Motion Prediction Equations

GMPEs, relating peak ground motions (especially acceleration and velocity) with earthquake magnitude, distance, and various other attributes of the earthquake, are key for seismic hazard analysis. Equations (10a)–(10c) together with an rms-to-peak relation may be combined to give first-order GMPEs for acceleration, velocity, and displacement. A previously adopted statistical theory, relating the signal's rms to its peak value, is restricted to $f_0 \ll f_\kappa$ (e.g., Baltay & Hanks, 2014; Vanmarcke & Lai, 1980). Because, however, this condition is not always met, an empirical approach is taken. Log-log diagrams of peak ground displacement (PGD), peak ground velocity (PGV), and peak ground acceleration (PGA) as functions of D_{rms}, V_{rms}, and A_{rms}, respectively, are shown in Figure 12. The following empirical relations are obtained:

$$\mathrm{PGD} = 2.1(\pm 0.7) D_{\mathrm{rms}}, \tag{19a}$$

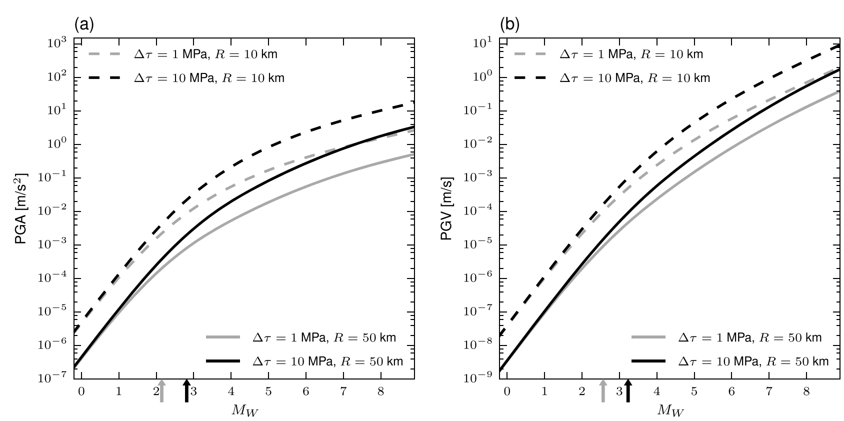

Figure 13. Peak ground (a) acceleration and (b) velocity as a function of magnitude (i.e., equations (20c) and (20b)), with κ = 0.03 s, and different values of stress drop and distance. The gray and black arrows adjacent to the magnitude axes mark the transition from the $\Delta\tau$-independent to the $\Delta\tau$-dependent regimes for $\Delta\tau$ = 1 MPa and $\Delta\tau$ = 10 MPa, respectively.

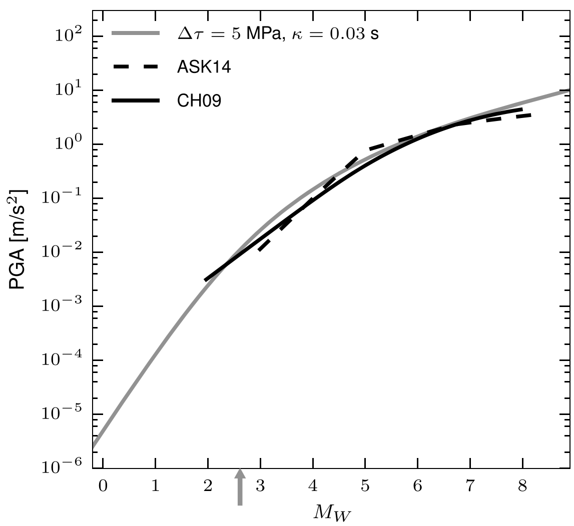

Figure 14. Comparison between the new peak acceleration GMPE (equation (20c), with $\Delta\tau$ = 5 MPa, κ = 0.03 s, and R = 10 km, solid gray curve) and those of Cua and Heaton (2009) (CU09, solid black curve), and Abrahamson et al. (2014) (ASK14, dashed black curve) with R = 10 km.

$$\mathrm{PGV} = 2.9(\pm 0.9)V_{\mathrm{rms}}, \tag{19b}$$

and:

$$\mathrm{PGA} = 3.3(\pm 0.9)A_{\mathrm{rms}}, \tag{19c}$$

in which the values inside the parentheses indicate one standard deviation. It is emphasized that because the rms of the ground motions are subject to the data intervals, so do the peak-to-rms proportions, and different schemes for setting the data intervals would result in different relations (Hanks & McGuire, 1981). The empirical relations in (19a)–(19c) combined with the theoretical results in (10a)–(10c) and the above expression for the data interval constitute semitheoretical GMPEs for PGD, PGV, and PGA:

$$\mathrm{PGD} = 2.1M_0^{5/6}\Delta\tau^{1/6}\frac{\beta_D}{R\sqrt{\frac{1}{kC_S}\left(\frac{7M_0}{16\Delta\tau}\right)^{1/3}+R/C_S}\left[1+0.5\pi^2\kappa kC_S\left(\frac{16\Delta\tau}{7M_0}\right)^{1/3}\right]^{1/2}}, \tag{20a}$$

$$\mathrm{PGV} = 2.9\sqrt{M_0\Delta\tau}\frac{\beta_V}{R\sqrt{\frac{1}{kC_S}\left(\frac{7M_0}{16\Delta\tau}\right)^{1/3}+R/C_S}\left[1+\pi^{4/3}\kappa kC_S\left(\frac{16\Delta\tau}{7M_0}\right)^{1/3}\right]^{3/2}}, \tag{20b}$$

$$\mathrm{PGA} = 3.3M_0^{1/3}\Delta\tau^{2/3}\frac{\beta_A}{R\sqrt{\kappa\left[\frac{1}{kC_S}\left(\frac{7M_0}{16\Delta\tau}\right)^{1/3}+R/C_S\right]}\left[1+1.5^{-1/4}\pi\kappa kC_S\left(\frac{16\Delta\tau}{7M_0}\right)^{1/3}\right]^{2}}. \tag{20c}$$

For hazard assessment, the stress drop in (20a)–(20c) may be substituted with a magnitude-dependent and/or region-specific functions, such as equations (18a) and (18b) (e.g., Archuleta & Ji, 2016; Trugman & Shearer, 2017).

PGA and PGV as a function of magnitude are shown in Figure 13 for hypocentral distances of 10 and 50 km, and for stress drops of 1 and 10 MPa. The arrows adjacent to the horizontal axes mark the transition from the $\Delta\tau$-independent to the $\Delta\tau$-dependent regimes (see discussion in reference to equations (11a)–(11c) and (12a)–(12c)). As already shown using stochastic simulations (Baltay & Hanks, 2014; Douglas & Jousset, 2011), the switch from one regime to another results in the peak shaking versus magnitude curves being steeper under the $\Delta\tau$-independent regime than under the $\Delta\tau$-dependent regime. This slope change is smaller for PGV as it is more magnitude-dependent than PGA (equations (11a)–(11c)). Additionally, the vertical separation between curves corresponding to different stress drops increases with increasing earthquake magnitude. Consequently, the PGA of sites located 10 km away from of a M_w 7 and $\Delta\tau$ = 1 MPa is the same as that experienced at a site that is 50 km away from an earthquake of the same magnitude, but a stress drop that is 10 times larger. A comparison between the new GMPE for PGA (equation (20c)) and those of Cua and Heaton (2009) and Abrahamson et al. (2014) reveals good agreement (Figure 14). The main advantage of the new GMPE with respect to empirical ones is that it is based on a simple widely adopted physical source model (attenuated Omega-square spectra). As such, it accounts for the three most important source parameters affecting ground motion intensity: the seismic moment, the hypocentral distance, and the stress drop. The effect of the latter has only recently been integrated into GMPEs (e.g., Ameri et al., 2017). The discrepancies between the (natural) logarithm of the observed and predicted PGA are shown in Figure 15 as a function of magnitude and distance, with predicted PGA calculated using $\Delta\tau$, M_0, and κ_0 obtained via the two-step inversion. That the discrepancy diagrams show no magnitude or distance dependencies indicate that the PGA to magnitude and distance relations are properly captured by the new GMPE and that the neglection of

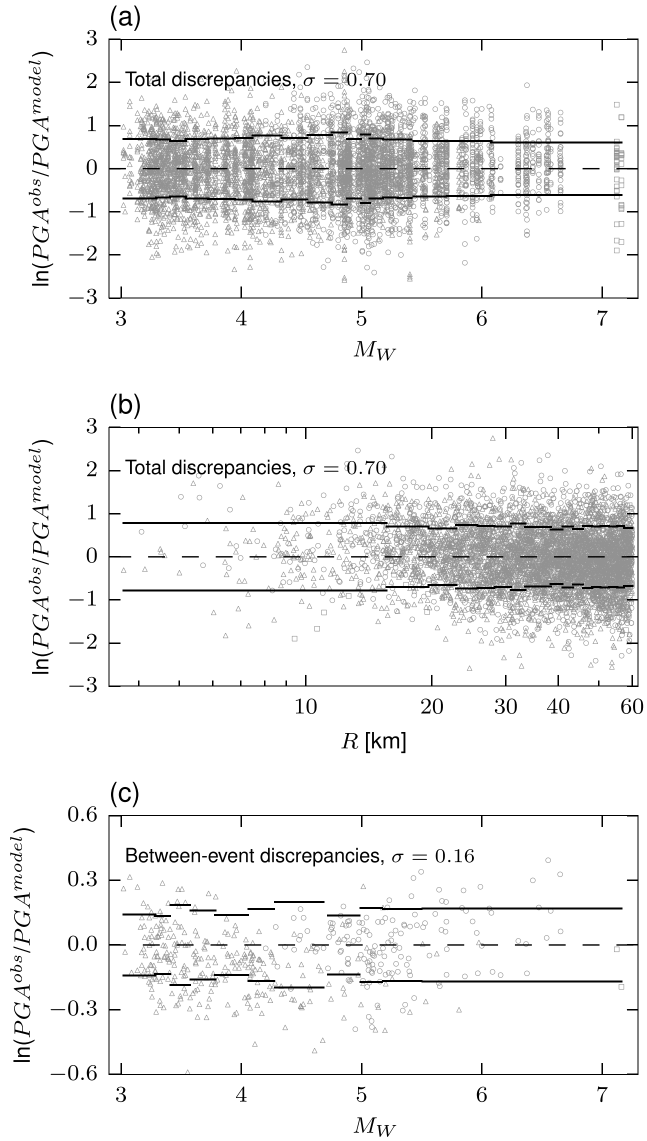

Figure 15. The discrepancies between the natural logarithm of the observed and predicted PGA. (a) The total discrepancies as a function of magnitude. (b) The total discrepancies as a function of distance. (c) The between-event discrepancies as a function of magnitude. The dashed lines indicate zero discrepancy, and the solid lines indicate one standard deviation, estimated per bin of 300 seismograms (panels a and b) or 40 events (panel c). Standard deviations are reported at the top-left corner of each panel.

anelastic attenuation is justified for the hypocentral distances considered in this study. The smallness of the between-event discrepancies (Figure 15c) highlights the benefit of accounting for stress drop effects in GMPEs. Because the between-event discrepancies are small, the within-event and the total discrepancies are nearly identical (therefore, the within-event discrepancies are not shown here). The total discrepancies of the new GMPE are comparable to recent empirically based GMPEs (e.g., Abrahamson et al., 2014; Boore et al., 2014; Bora et al., 2015; Campbell & Bozorgnia, 2014; Chiou & Youngs, 2014; Idriss, 2014), which account for numerous additional effects that are not considered here.

6. Conclusions

Theoretical equations relating the rms of the far-field ground motions (displacement, velocity and acceleration) with earthquake source parameters and attenuation were derived using the omega-squared model

(Brune, 1970). Apart from providing useful insight into how source and site parameters control earthquake ground motions, these model-based predictions may also be exploited for earthquake source parameters inversion and ground motion prediction.

A new approach for inverting the source spectral parameters is introduced. The main advantage of this method is the circumventing of the time domain to frequency domain transformation and consequently also the spectral modeling intricacies. An additional advantage of the new scheme is that it yields more robust and more stable source parameters than those obtained using the frequency domain approach (Figure 8).

Finally, a set of physics-based GMPEs for displacement, velocity, and acceleration is derived (equations (20a)–(20c)) that is shown to be in good agreement with recent empirical GMPEs (Figure 14). Unlike previous region-specific GMPEs, containing numerous empirically tuned coefficients, the new GMPEs are extremely simple and are readily implementable worldwide, even in low-seismicity regions, where the data set available for setting the many degrees of freedom in the GMPE is of limited size.

Acknowledgments

We thank the Editor, Yehuda Ben-Zion, and the Associate Editor, Yoshihiro Kaneko, for their work and insightful comments. We also thank Fabrice Cotton and an anonymous reviewer for their very constructive remarks. The data used in this study were obtained from the Southern California Earthquake Data Center (Caltech Data Set. http://scedc.caltech.edu/; last accessed on January 2016), the K-NET and KiK-net strong motion networks (http://www.kyoshin.bosai.go.jp/; last accessed on January 2016), and from PEER Ground Motion Database (http://ngawest2.berkeley.edu/site/; last accessed on January 2016).

References

Abrahamson, N. A., Silva, W. J., & Kamai, R. (2014). Summary of the ASK14 ground motion relations for active crustal regions. *Earthquake Spectra*, *30*(3), 1025–1055. https://doi.org/10.1193/070913EQS198M

Allmann, B. P., & Shearer, P. M. (2009). Global variations of stress drop for moderate to large earthquakes. *Journal of Geophysical Research*, *114*, B01310. https://doi.org/10.1029/2008JB005821

Ameri, G., Drouet, S., Traversa, P., Bindi, D., & Cotton, F. (2017). Toward an empirical ground motion prediction equation for France: Accounting for regional differences in the source stress parameter. *Bulletin of Earthquake Engineering*, *15*(11), 4681–4717. https://doi.org/10.1007/s10518-017-0171-1

Anderson, J. G., & Hough, S. E. (1984). A model for the shape of the Fourier amplitude spectrum of acceleration at high frequencies. *Bulletin of the Seismological Society of America*, *74*, 1969–1993.

Archuleta, R. J., & Ji, C. (2016). Moment rate scaling for earthquakes 3.3 ≤ M ≤ 5.3. *Geophysical Research Letters*, *43*, 12,004–12,011. https://doi.org/10.1002/2016GL071433

Baltay, A., & Hanks, T. C. (2014). Understanding the magnitude dependence of PGA and PGV in NGA-West 2 data. *Bulletin of the Seismological Society of America*, *104*, 2851–2865. https://doi.org/10.1785/0120130283

Baltay, A., Ide, S., Prieto, G., & Beroza, G. (2011). Variability in earthquake stress drop and apparent stress. *Geophysical Research Letters*, *38*, L06303. https://doi.org/10.1029/2011GL046698

Boore, D. M., Stewart, J. P., Seyhan, E., & Atkinson, G. M. (2014). NGA-West2 equations for predicting PGA, PGV, and 5% damped PSA for shallow crustal earthquakes. *Earthquake Spectra*, *30*(3), 1057–1085. https://doi.org/10.1193/070113EQS184M

Boore, D. M., & Thompson, E. M. (2014). Path durations for use in the stochastic-method simulation of ground motions. *Bulletin of the Seismological Society of America*, *104*, 2541–2552. https://doi.org/10.1785/0120140058

Bora, S. S., Scherbaum, F., Kuehn, N., Stafford, P. J., & Edwards, B. (2015). Development of a response spectral ground-motion prediction equation (GMPE) for seismic hazard analysis from empirical Fourier spectral and duration models. *Bulletin of the Seismological Society of America*, *105*(4), 2192–2218. https://doi.org/10.1785/0120140297

Brune, J. N. (1970). Tectonic stress and the spectra of seismic shear waves from earthquakes. *Journal of Geophysical Research*, *75*, 4997–5009. https://doi.org/10.1029/JB075i026p04997

Campbell, K. W., & Bozorgnia, Y. (2014). NGA-West2 ground motion model for the average horizontal components of PGA, PGV, and 5% damped linear acceleration response spectra. *Earthquake Spectra*, *30*(3), 1087–1115. https://doi.org/10.1193/062913EQS175M

Chen, X., & Shearer, P. M. (2011). Comprehensive analysis of earthquake source spectra and swarms in the Salton Trough, California. *Journal of Geophysical Research*, *116*, B09309. https://doi.org/10.1029/2011JB008263

Chiou, B. S.-J., & Youngs, R. R. (2014). Update of the Chiou and Youngs NGA model for the average horizontal component of peak ground motion and response spectra. *Earthquake Spectra*, *30*(3), 1117–1153. https://doi.org/10.1193/072813EQS219M

Cua, G., & Heaton, T. H. (2009). Characterizing average properties of Southern California ground motion amplitudes and envelopes. Earthquake Engineering Research Laboratory, Pasadena, California.

Dong, G., & Papageorgiou, A. S. (2002). Seismic radiation from a unidirectional asymmetrical circular crack model, Part II: Variable rupture velocity. *Bulletin of the Seismological Society of America*, *92*(3), 962–982. https://doi.org/10.1785/0120010209

Douglas, J., & Jousset, P. (2011). Modeling the differences in ground motion magnitude-scaling in small and large earthquakes. *Seismological Research Letters*, *82*(4), 504–508. https://doi.org/10.1785/gssrl.82.4.504

Drouet, S., Bouin, M.-P., & Cotton, F. (2011). New moment magnitude scale, evidence of stress drop magnitude scaling and stochastic ground motion model for the French West Indies. *Geophysical Journal International*, *187*(3), 1625–1644. https://doi.org/10.1111/j.1365-246X.2011.05219.x

Edwards, B., Ktenidou, O.-J., Cotton, F., Abrahamson, N., Van Houtte, C., & Fäh, D. (2015). Epistemic uncertainty and limitations of the κ0 model for near-surface attenuation at hard rock sites. *Geophysical Journal International*, *202*(3), 1627–1645. https://doi.org/10.1093/gji/ggv222

Eshelby, J. D. (1957). The determination of the elastic field of an ellipsoidal inclusion, and related problems. *Proceedings of the Royal Society of London A: Mathematical, Physical and Engineering Sciences*, *241*, 376–396. https://doi.org/10.1098/rspa.1957.0133

Hanks, T. C. (1982). fmax. *Bulletin of the Seismological Society of America*, *72*, 1867–1879.

Hanks, T. C., & McGuire, R. K. (1981). The character of high-frequency strong ground motion. *Bulletin of the Seismological Society of America*, *71*, 2071–2095.

Ide, S., & Beroza, G. C. (2001). Does apparent stress vary with earthquake size? *Geophysical Research Letters*, *28*(17), 3349–3352. https://doi.org/10.1029/2001GL013106

Ide, S., Beroza, G. C., Prejean, S. G., & Ellsworth, W. L. (2003). Apparent break in earthquake scaling due to path and site effects on deep borehole recordings. *Journal of Geophysical Research*, *108*(B5), 2271. https://doi.org/10.1029/2001JB001617

Idriss, I. M. (2014). An NGA-West2 empirical model for estimating the horizontal spectral values generated by shallow crustal earthquakes. *Earthquake Spectra*, *30*(3), 1155–1177. https://doi.org/10.1193/070613EQS195M

Izutani, Y., & Kanamori, H. (2001). Scale-dependence of seismic energy-to-moment ratio for strike-slip earthquakes in Japan. *Geophysical Research Letters*, *28*(20), 4007–4010. https://doi.org/10.1029/2001GL013402

Kanamori, H., & Anderson, D. L. (1975). Theoretical basis of some empirical relations in seismology. *Bulletin of the Seismological Society ofAmerica*, *65*(5), 1073–1095.

Kaneko, Y., & Shearer, P. M. (2015). Variability of seismic source spectra, estimated stress drop, and radiated energy, derived from cohesive-zone models of symmetrical and asymmetrical circular and elliptical ruptures. *Journal of Geophysical Research: Solid Earth*, *120*, 1053–1079. https://doi.org/10.1002/2014JB011642

Ktenidou, O.-J., Cotton, F., Abrahamson, N., & Anderson, J. G. (2014). Taxonomy of κ: A review of definitions and estimation approaches targeted to applications. *Seismological Research Letters*, *85*, 135–146. https://doi.org/10.1785/0220130027

Leyton, F., Ruiz, J., Campos, J., & Kausel, E. (2009). Intraplate and interplate earthquakes in Chilean subduction zone: A theoretical and observational comparison. *Physics of the Earth and Planetary Interiors*, *175*(1–2), 37–46. https://doi.org/10.1016/j.pepi.2008.03.017

Lior, I., & Ziv, A. (2017). The relation between ground acceleration and earthquake source parameters: Theory and observations. *Bulletin of the Seismological Society of America*, *107*, 1012–1018. https://doi.org/10.1785/0120160251

Lior, I., Ziv, A., & Madariaga, R. (2015). P-wave attenuation with implications for earthquake early warning. *Bulletin of the Seismological Society of America*, *106*, 13–22. https://doi.org/10.1785/0120150087

Madariaga, R. (1976). Dynamics of an expanding circular fault. *Bulletin of the Seismological Society of America*, *65*, 163–182.

Mayeda, K., Malagnini, L., & Walter, W. R. (2007). A new spectral ratio method using narrow band coda envelopes: Evidence for non-self-similarity in the Hector Mine sequence. *Geophysical Research Letters*, *34*, L11303. https://doi.org/10.1029/2007GL030041

Mayor, J., Bora, S. S., & Cotton, F. (2018). Capturing regional variations of hard-rock κ0 from coda analysis. *Bulletin of the Seismological Society of America*, *108*(1), 399–408. https://doi.org/10.1785/0120170153

Nakano, K., Matsushima, S., & Kawase, H. (2015). Statistical properties of strong ground motions from the generalized spectral inversion of data observed by K-NET, KiK-net, and the JMA Shindokei Network in Japan. *Bulletin of the Seismological Society of America*, *105*(5), 2662–2680. https://doi.org/10.1785/0120140349

Oth, A., Bindi, D., Parolai, S., & Giacomo, D. D. (2010). Earthquake scaling characteristics and the scale-(in) dependence of seismic energy-to-moment ratio: Insights from KiK-net data in Japan. *Geophysical Research Letters*, *37*, L19304. https://doi.org/10.1029/2010GL044572

Oth, A., Bindi, D., Parolai, S., & Giacomo, D. D. (2011). Spectral analysis of K-NET and KiK- net data in Japan, Part II: On attenuation characteristics, source spectra, and site response of borehole and surface stations. *Bulletin of the Seismological Society of America*, *101*, 667–687. https://doi.org/10.1785/0120100135

Prieto, G. A., Shearer, P. M., Vernon, F. L., & Kilb, D. (2004). Earthquake source scaling and self-similarity estimation from stacking P and S spectra. *Journal of Geophysical Research*, *109*, B08310. https://doi.org/10.1029/2004JB003084

Ross, Z. E., & Ben-Zion, Y. (2016). Toward reliable automated estimates of earthquake source properties from body wave spectra. *Journal of Geophysical Research: Solid Earth*, *121*, 4390–4407. https://doi.org/10.1002/2016JB013003

Sato, T., & Hirasawa, T. (1973). Body wave spectra from propagatingshear cracks. *Journal of Physics of the Earth*, *21*, 415–431.

Scholz, C. H., Aviles, C. A., & Wesnousky, S. G. (1986). Scaling differences between large interplate and intraplate earthquakes. *Bulletin of the Seismological Society of America*, *76*(1), 65–70.

Shearer, P. M., Prieto, G. A., & Hauksson, E. (2006). Comprehensive analysis of earthquakes source spectra in southern California. *Journal of Geophysical Research*, *111*, B06303. https://doi.org/10.1029/2005JB003979

Takahashi, T., Sato, H., Ohtake, M., & Obara, K. (2005). Scale dependence of apparent stress for earthquakes along the subducting Pacific plate in Northeastern Honshu, Japan. *Bulletin of the Seismological Society of America*, *95*(4), 1334–1345. https://doi.org/10.1785/0120040075

Trugman, D. T., & Shearer, P. M. (2017). Application of an improved spectral decomposition method to examine earthquake source scaling in Southern California. *Journal of Geophysical Research: Solid Earth*, *122*, 2890–2910. https://doi.org/10.1002/2017JB013971

Van Houtte, C., Drouet, S., & Cotton, F. (2011). Analysis of the origins of κ (kappa) to compute hard rock to rock adjustment factors for GMPEs. *Bulletin of the Seismological Society of America*, *101*, 2926–2941. https://doi.org/10.1785/0120100345

Vanmarcke, E. H., & Lai, S. S. (1980). Strong-motion duration and RMS amplitude of earthquake records. *Bulletin of the Seismological Society of America*, *70*, 1293–1307.

Wu, Y. M., Allen, R. M., & Wu, C. F. (2005). Revised ML determination for crustal earthquakes in Taiwan. *Bulletin of the Seismological Society of America*, *95*, 2517–2524. https://doi.org/10.1785/0120050043

Wu, Y. M., & Zhao, L. (2006). Magnitude estimation using the first three seconds P-wave amplitude in earthquake early warning. *Geophysical Research Letters*, *33*, L16312. https://doi.org/10.1029/2006GL026871

Ziv, A., & Lior, I. (2016). Real-time moment magnitude and stress drop with implications for real-time shaking prediction. *Bulletin of the Seismological Society of America*, *106*, 2459–2468. https://doi.org/10.1785/0120160091